Chapter 5 Structural, Optical and magnetic properties of $CeCr_{1-x}Fe_xO_3$ ($0.2 \leq x \leq 0.5$) nanoparticles

5.1 Introduction

In this chapter, we have conducted an investigation on the structural modification and magnetic properties of $CeCr_{1-x}Fe_xO_3$ with changing Fe concentration (x) from 0.2 to 0.5, synthesized using the solution combustion method. XRD pattern confirm the phase pure orthorhombic structure. Rietveld fitting of XRD patterns shows a linear increase in the lattice parameters (a, b, and c) and volume, particle size as x increases from 0.2 to 0.5, which is thoroughly discussed in Section 5.2. In section 5.3, elemental analysis has been shown and reveal the formation of Fe^{2+} and Cr^{6+} along with Fe^{3+} and Cr^{3+} in synthesized sample. Moving to the section 5.4, we present optical properties particularly the band gap using Tauc plot. We demonstrate decrease in band gap from 2.48 to 1eV as x increases. Magnetization properties is discussed by using out the magnetization vs. temperature plot and field. An increase in spin reorientation temperatures T_{SR1} and T_{SR2} from 62 K to 138 K and 37 K to 83 K, respectively, is detected as x increases from 0.2 to 0.5. This increase in T_{SR1} and T_{SR2} can be attributed to the enhanced Ce^{3+}-Fe^{3+} and Fe^{3+}-Fe^{3+} magnetic interactions resulting from the substitution of Fe as discussed in section 5.5.1. Furthermore, Section 5.5.2 presents the magnetization vs. field analysis, which reveals an initial rise in coercivity up to T_{SR1}, followed by a subsequent decrease with increasing temperature irrespective of compositions. In section 5.6, we summarized all the important findings.

5.2 Structural and microstructural analysis

Figure. 5.1 shows the room temperature powder XRD patterns of $CeCr_{1-x}Fe_xO_3$ $(0.2 \leq x \leq 0.5)$ in the 2θ range of 10°–120°.

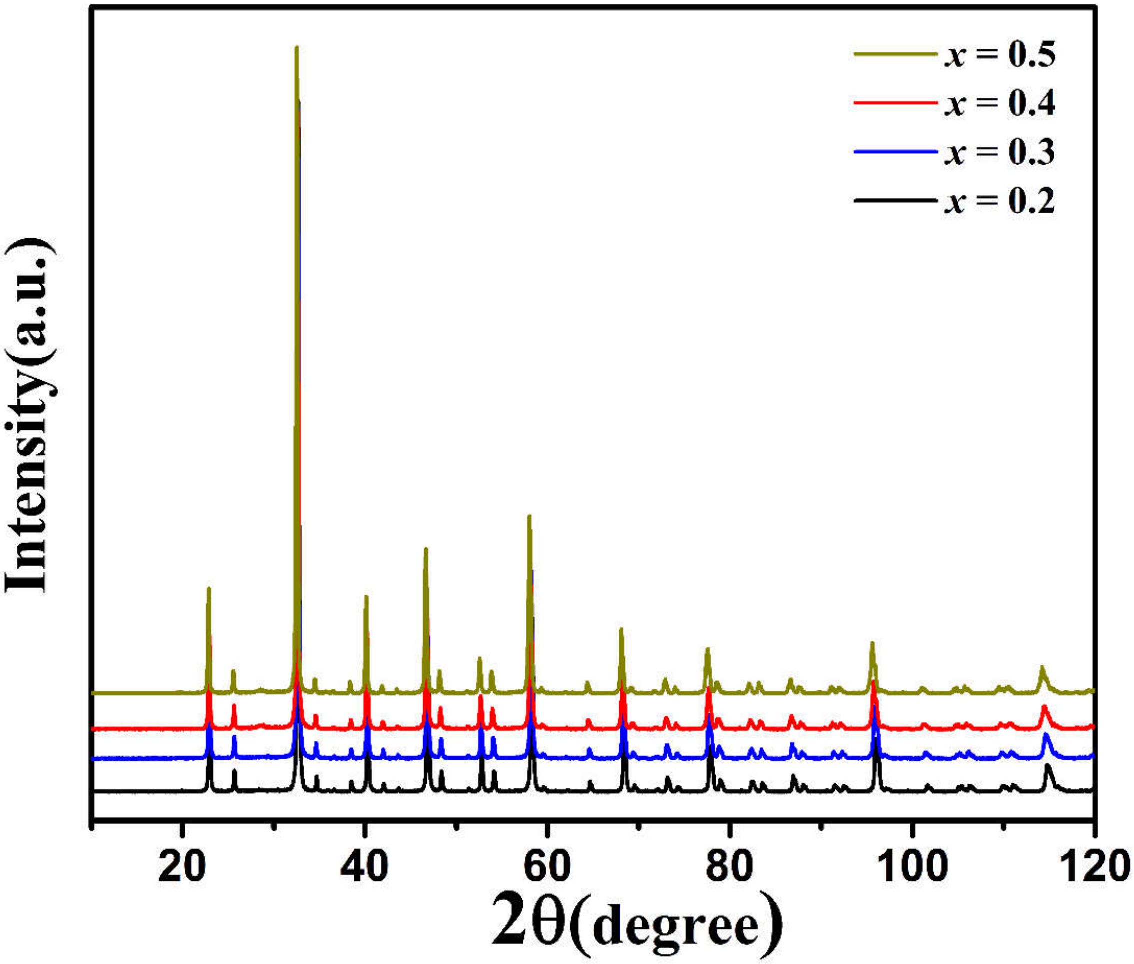

Figure 5.1 X-ray diffraction pattern of $CeCr_{1-x}Fe_xO_3(0.2 \leq x \leq 0.5)$.

Sharp and well resolved diffraction peaks indicate the crystalline nature of particles. The observed diffraction peaks are indexed based on the JCPDS card # 898770 for the space group, *Pnma* in orthorhombic structure. In X-ray diffraction patterns, no other peak is observed corresponding to any impurity phase after substitution of Fe, confirming the pure orthorhombic one. Further, XRD patterns are analyzed by Rietveld refinement using Full proof program (figure.5.2 (a-d)). The fit between the experimentally observed and calculated diffraction profiles are quite excellent and confirm the orthorhombic structure irrespective composition. The refined structural parameters for $CeCr_{1-x}Fe_xO_3$ ($x = 0.2$ to 0.5) are listed in Table 5.1. The lattice parameter a, b and c increases linearly when x increases from 0.2 to 0.5 (figure.5.2 (e-f)). The unit cell volume also increases linearly from 233.746 Å^3 for x = 0.2 to 236.18 Å^3 for $x = 0.5$ (figure.5.2g). The increment in lattice parameters and unit cell volume thus suggest that Cr^{3+} ions with ionic radius 0.615 Å substitutes the Fe^{3+} ion with ionic radius of 0.645Å suitably. From Table 5.1, we have observed that bond angle, ∠Cr–O1–Cr decreases from 156.38° to 154.66° when x increases from 0.2 to 0.5. However ∠Cr-O2-Cr increases from 157.6° to 157.8° when x increases from 0.2 to 0.4 and show a drop upto 156.9° at $x = 0.5$. With the incorporation of Fe, the average bond length of <Cr-O> and <Ce-O> increases for all composition except a decrease in <Ce-O> at $x = 0.5$. The Goldschmidt tolerance factor t, estimated using $t = \langle Ce\text{-}O \rangle / \{\sqrt{2}(< Cr - O >)\}$, is found to be 0.910 for $x = 0.2$ and decreases to 0.905 when $x = 0.5$ without any significant variation in 't' for the intermediate compositions. Evidently, the decrease in the tolerance factor suggests that the increase in x leads to more distortion in orthorhombic structure.

Table 5.1 Structural parameter extracted from Rietveld refinement of XRD pattern of $CeCr_{1-x}Fe_xO_3$ ($0.2 \leq x \leq 0.5$).

Compound	**x = 0.2**	**x = 0.3**	**x = 0.4**	**x = 0.5**
a	5.4928(1)	5.5019(1)	5.5114(1)	5.5185(1)
b	7.7508(2)	7.7601(2)	7.7690(1)	7.7772(2)
c	5.4903(1)	5.4948(1)	5.4995(1)	5.5029(1)
V	233.746	234.608	235.483	236.180
Ce				
x	0.0305(1)	0.0316(1)	0.0323(1)	0.03259(1)
y	0.25	0.25	0.25	0.25
z	-0.0067(2)	-0.0069(2)	-0.0069(2)	-0.0071(2)
B_{iso}(Å^2)	0.134	0.134	0.134	0.134
Cr/Fe				
x	0.00	0	0	0
y	0.00	0	0	0
z	0.50	0.5	0.5	0.5
B_{iso}(Å^2)$_{Cr}$	0.233	0.233	0.233	0.233
B_{iso}(Å^2)$_{Fe}$	0.232	0.232	0.232	0.232
O1				
x	0.4874(13)	0.4857(15)	0.4869(15)	0.4851(15)
y	0.25	0.25	0.25	0.25
z	0.072(2)	0.075(2)	0.076(2)	0.078(2)
B_{iso}(Å^2)	0.450	0.450	0.450	0.450
O2				
x	0.284(2)	0.284(3)	0.284(2)	0.289(2)
y	0.0358(10)	0.0346(11)	0.0348(12)	0.0335(11)
z	0.713(2)	0.713(2)	0.715(2)	0.716(2)
B_{iso}(Å^2)	0.450	0.450	0.450	0.450
Cr(Fe)-O1-Cr(Fe)	156.38(9)	155.59(9)	155.36(10)	154.66(10)
Cr(Fe)-O2-Cr(Fe)	157.2(4)	157.6(4)	157.8(4)	156.9(4)
Cr(Fe)-O1	1.980(2)	1.985(2)	1.988(2)	1.993(2)
Cr(Fe)-O2	1.970(10)	1.971(11)	1.980(11)	2.011(10)
Cr(Fe)-O2’	1.991(10)	1.993(11)	1.987(11)	1.966(11)
<Cr-O>	1.980	1.983	1.985	1.990
<Ce-O>	2.5488	2.5478	2.5506	2.547
‘t’	0.910	0.908	0.908	0.905

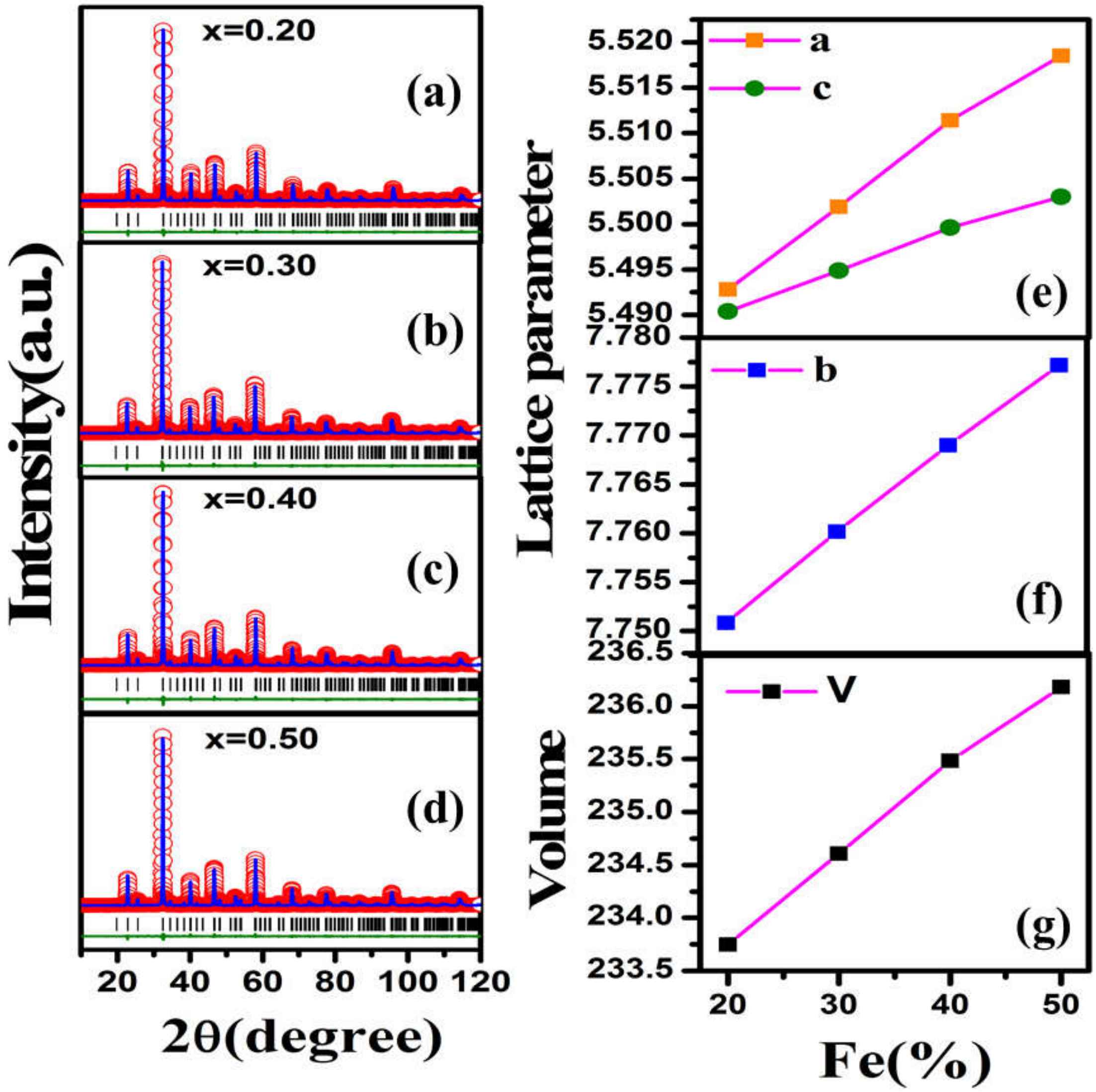

Figure 5.2 (a), (b), (c), (d) Rietveld refinement of XRD pattern of $CeCr_{1-x}Fe_xO_3$($x = 0.2$ to 0.5) and (e)(f)(g) its structural parameter.

The size and morphology of typical compositions such as $CeCr_{1-x}Fe_xO_3$ (x = 0.2 and 0.4) nanoparticles are determined using the TEM micrographs. The particles are found to be agglomerated and deviated from spherical shape (figure 5.3). A typical particle size distribution histogram reveals the average particle size is ~69 nm and 81 nm for x = 0.2 nm and x = 0.4, respectively (figure 5.3).

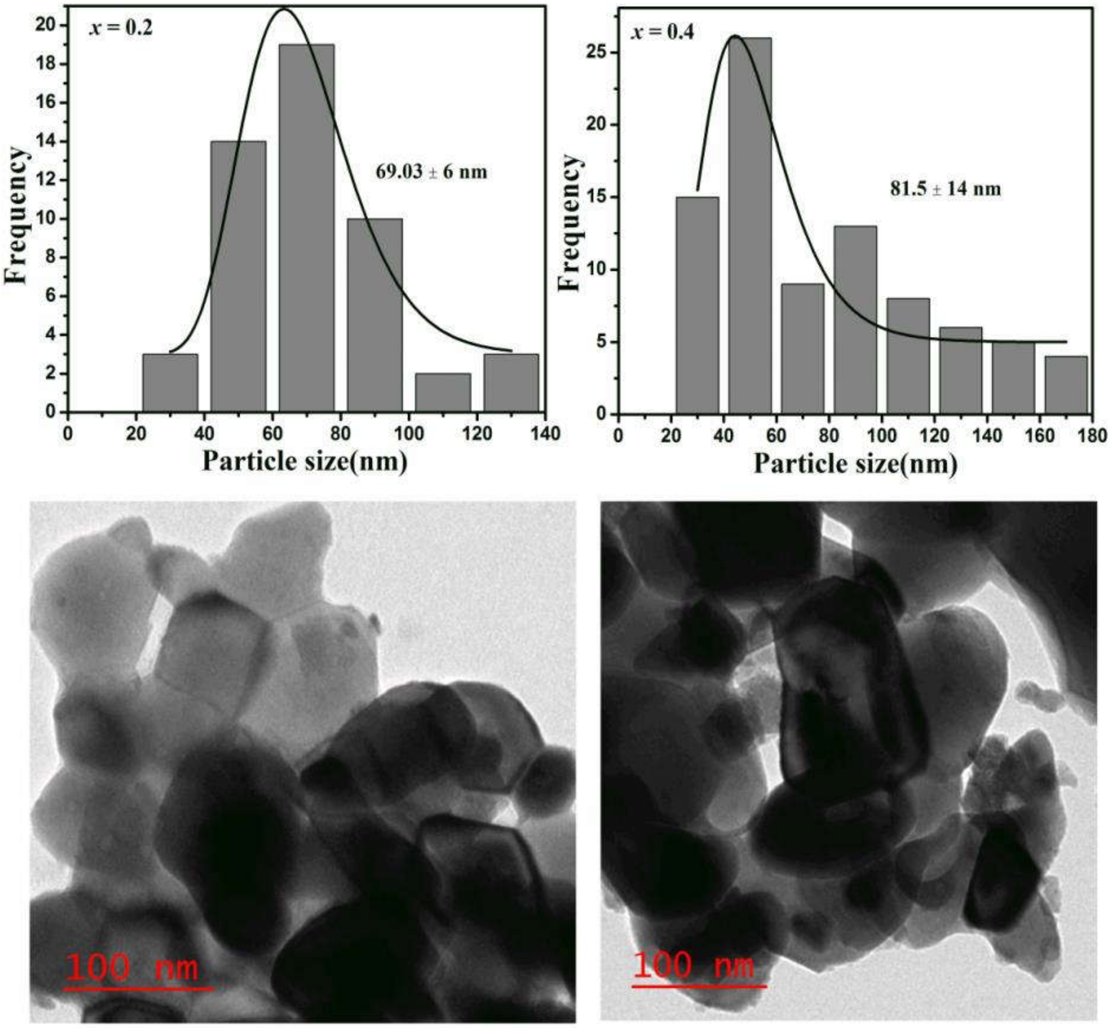

Figure 5.3 Transmission electron micrograph and particle distribution histogram of $CeCr_{1-x}$ Fe_xO_3 (x = 0.2 and 0.4).

5.3 Elemental analysis

Further, to confirm the oxidation states, we have carried out the XPS of $CeCr_{1-x}Fe_xO_3$ (x = 0.2 and 0.4). Figure 5.4 depicts the XPS spectra of $CeCr_{1-x}Fe_xO_3$ (x = 0.2 and 0.4) collected using Al Kα radiation.

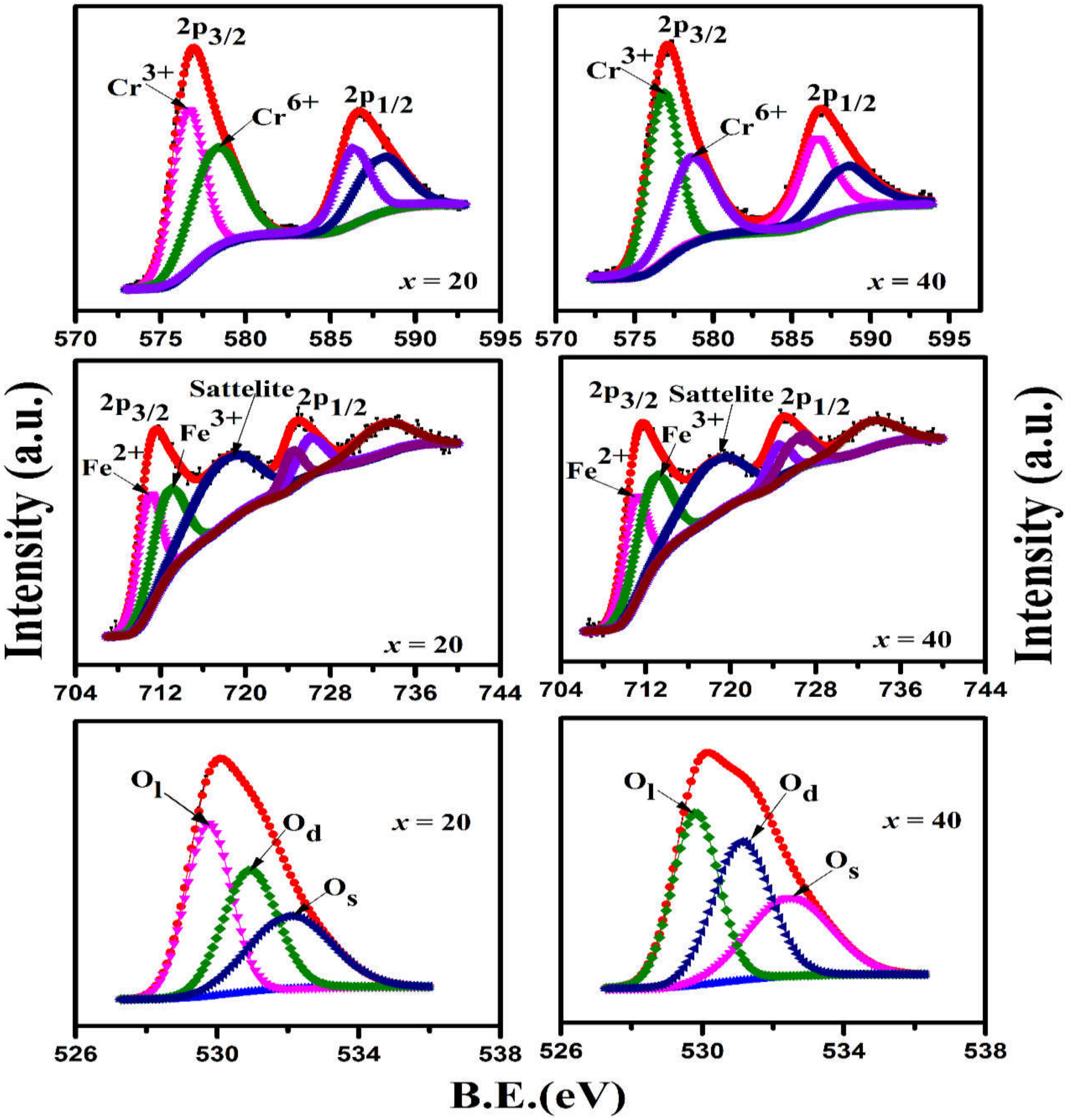

Figure 5.4 The fitted XPS spectra of Cr 2p, Fe2p and O1s of samples $CeCr_{1-x}Fe_xO_3$ (x = 0.2 and 0.4).

The core level binding energies are corrected with the carbon binding energy of 284.6 eV. The asymmetric peaks of Cr 2*p*, Fe 2*p*, and O 1*s* are fitted with a mixed Gaussian and Lorentzian functions using XPS peak (4.1) software. The two components observed in Cr spectra at ~576 and ~579 eV correspond to the $Cr^{3+}$and Cr^{6+}, respectively. The peaks in Fe spectra at ∼710 and ∼713 eV correspond to Fe^{2+} and Fe^{3+}, respectively. The asymmetric O1*s* core level spectra of oxygen around ∼529 eV are fitted with three peaks such as O_l, O_d and O_s using mixed Gaussian and Lorentzian functions as shown in Figure5.4. While O_l peak located at 529 eV is ascribed to the lattice oxygen atoms, O_d peak centered at ∼531 eV is due to the deficiency of oxygen followed by a small peak, Os, at ∼532 eV which is partly from the hydroxyl groups and from the chemisorbed oxygen lying on the surface of the samples. From the integrated area of Cr 2p, Fe 2p, and O 1s peak, the estimated ratio corresponding to Fe^{2+}/ Fe^{3+} and Cr^{6+}/Cr^{3+} demonstrates that Fe^{2+} and Cr^{6+} content increases along with oxygen vacancy when x increases from $x = 0.2$ to 0.4. While the presence of Cr^{6+} decreases the oxygen vacancies, Fe^{2+} enhances oxygen vacancies. The increase in oxygen vacancies with increase in x thus suggest that conversion of Fe^{3+} to Fe^{2+} dominates over the conversion of Cr^{3+} to Cr^{6+}. Further, the presence of Fe^{2+} dominates is evidenced from the increase in lattice parameter and volume also. Because, the ionic radius of Fe^{2+} is 0.785 Å which is significantly higher than the ionic radius of Cr^{6+} i.e. 0.44 Å. Hence, we establish that with increase in Fe concentration, conversion of Fe^{3+} to Fe^{2+} is more than that of Cr^{3+} to Cr^{6+} and hence accompanied with increase in lattice volume.

5.4 Optical properties

Further, to understand the effect of the Fe substitution in d–d transitions of Cr^{3+} site with the ground state 4F (t^3_{2g} e^0g) in CrO_6 octahedra, diffuse reflectance spectra in the extended visible range of 200 to 800 nm are recorded. Applying the Kubelka–Munk (KM) function, the diffuse reflectance spectra of $CeCr_{1-x}Fe_xO_3$ ($0.2 \leq x \leq 0.5$) is converted into absorption spectra and are plotted in figure 5.5.

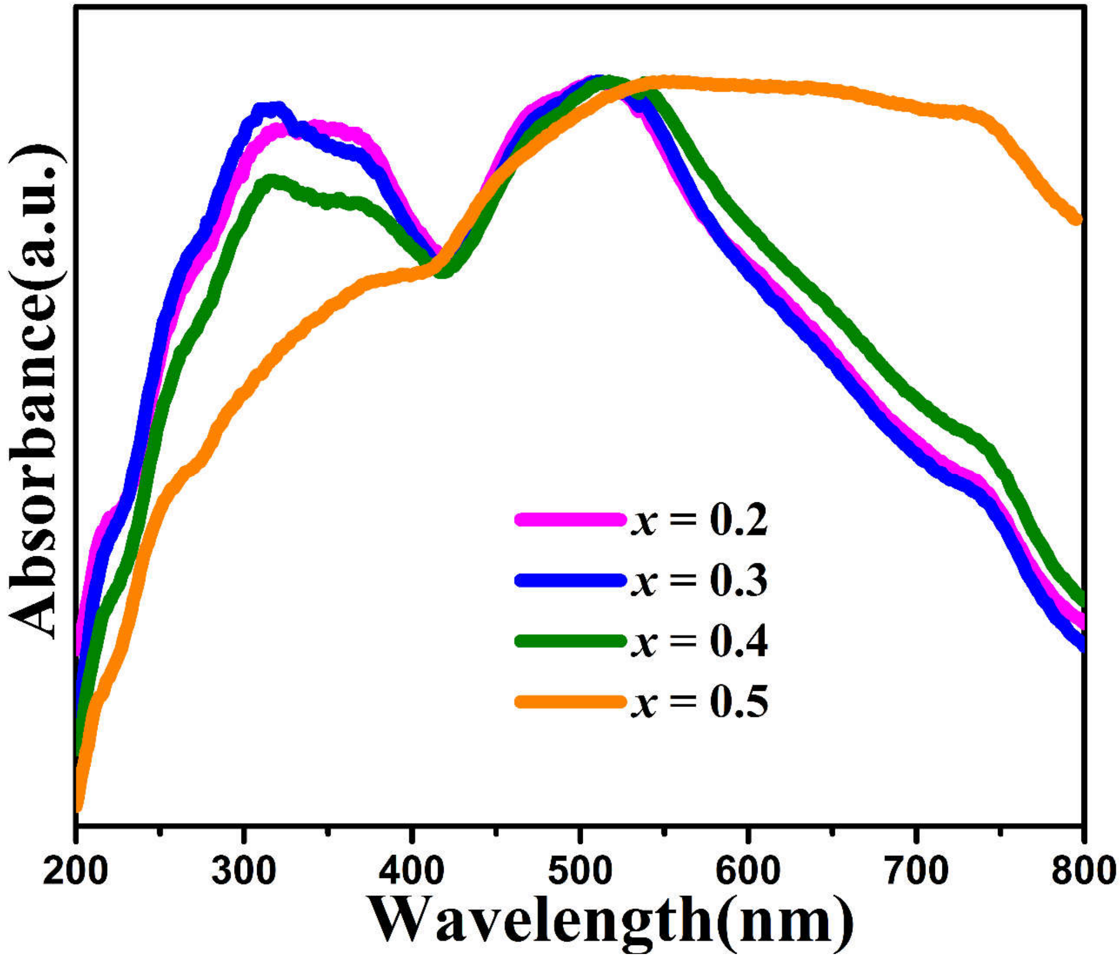

Figure 5.5 UV visible absorbance spectroscopy of $CeCr_{1-x}Fe_xO_3$($0.2 \leq x \leq 0.5$).

The peak at ~ 320 nm can be attributed to 4f to 5d charge transfer transition [113]. The absorption bands at around 500 nm can be attributed to the $^4A_{2g}$ *to* $^4T_{1g}$ transition (corresponding to 455.5 nm) of Cr^{3+} ion octahedral coordination and $^5T_{2g}$ to ^5E_g (corresponding to 550 nm) transition of Fe^{2+} octahedral coordination [77,114]. While the absorption band observed at ~ 640 nm can be attributed to$^4A_{2g}$ *to* $^4T_{2g}$ transition in Cr^{3+} octahedral complexes, the band observed at ~ 740 nm could be attributed to $^4A_{2g}$ *to* ^2E_g in the same Cr^{3+} octahedral complexes. The absorption band at ~ 740 is also possibly contributed by charge transfer from O^{2-} to Cr^{6+}, which lies near red region near IR. Fe^{3+} in octahedral coordination with d^5 configuration has no spin allowed transition, therefore, no transition due Fe^{3+} is contributed in absorption spectrum. The band gap calculated from tauc equation-

$$\alpha h\nu = A\left(h\nu - E_g\right)^{1/2} \qquad [5.1]$$

Here α is absorption coefficient, hν is the incident photon energy, A is a characteristic parameter, and n = 1/2 for direct transitions. $(\alpha h\nu)^2$ versus $h\nu$ for the three samples are plotted based on this equation, and shown in figure 5.6. The linear absorption edge curve are fitted with a straight line, the intersection of which with the $(\alpha h\nu)^2 = 0$ axis gives E_g as ~2.56, 2.52, 2.38 and 1.15 eV for $x = 0.2$, 0.3, 0.4 and 0.5, respectively. It is found that the band gap decreases from 2.47 to 1 eV with increase in x from 0.2 to 0.5, can be attributed to the increase in Fe^{2+}/Fe^{3+} concentration or increase in particle size with substitution of Fe [122]. Thus, it can be clearly seen that the band gap of $CeCrO_3$ may be simply tuned by Fe substitution at Cr-site doping, manifest its potential application as a photo-catalyst.

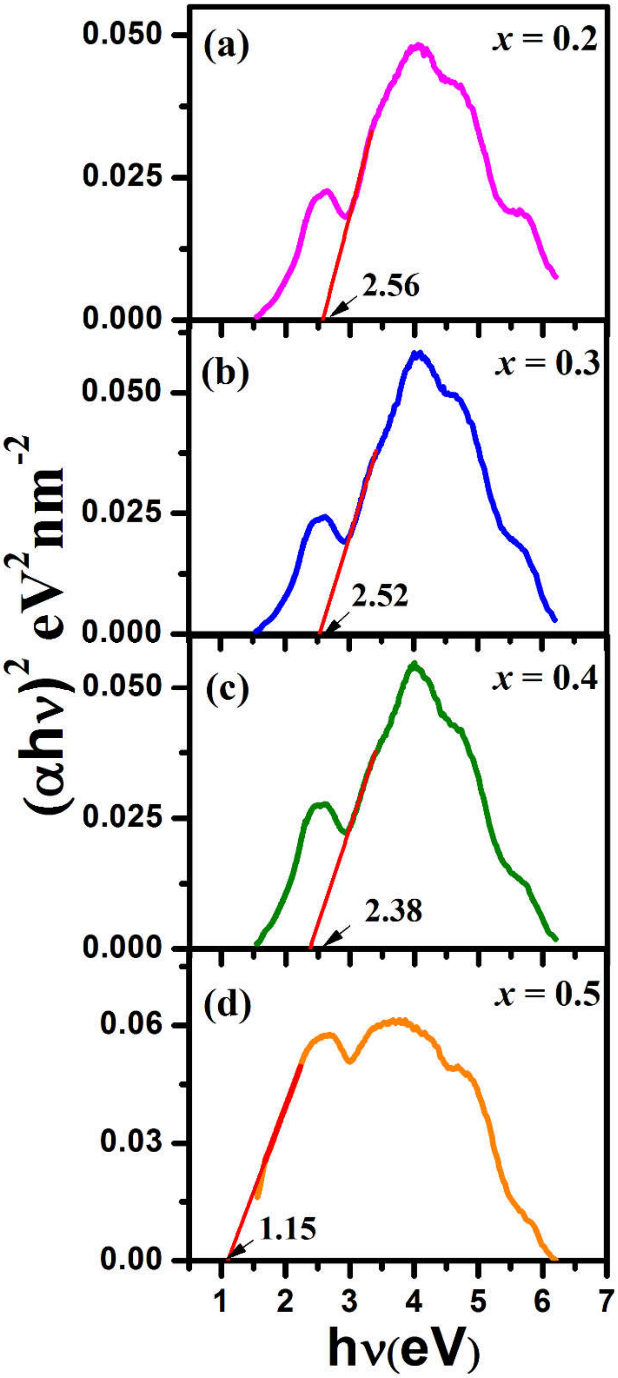

Figure 5.6 Analysis of band gaps from the absorbance spectra of $CeCr_{1-x}Fe_xO_3$ for $0.2 \leq x \leq 0.5$: (a) $x = 0.2$, (b) $x = 0.3$, (c) $x = 0.4$, (d) $x = 0.5$.

5.5 Magnetic properties

5.5.1 Temperature dependent magnetization

Temperature dependent magnetization curve recorded under 0.5 kOe field cooled and zero field cooled mode of $CeCr_{1-x}Fe_xO_3$ ($0.2 \leq x \leq 0.5$) are shown in Figure 5.7.

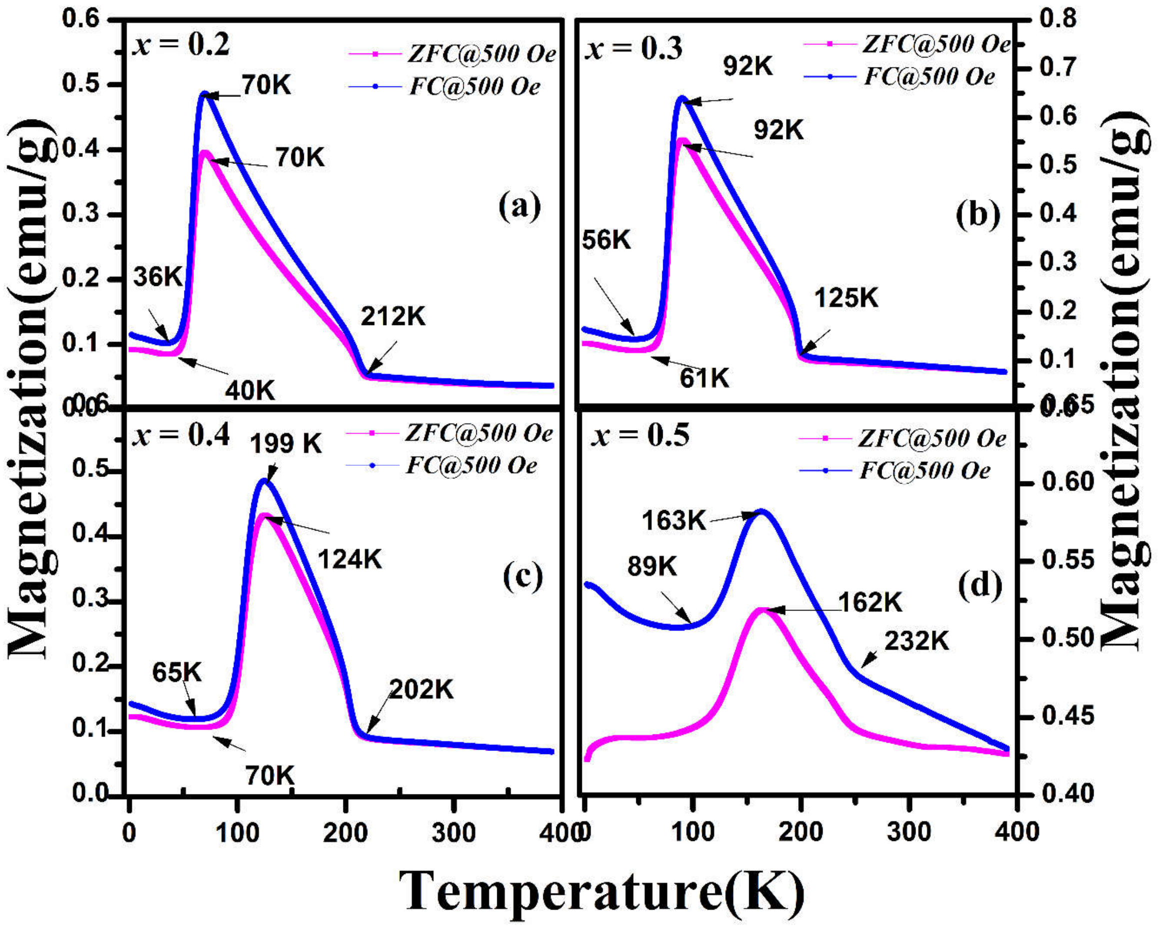

Figure 5.7 Magnetization v/s Temperature plot of $CeCr_{1-x}Fe_xO_3$($0.2 \leq x \leq 0.5$) at 0.5 kOe in field cooled and zero field cooled mode.

The magnetization curves are recorded from 390 K to 2 K for all composition. With decrease in temperature from 390 K, the field cooled magnetization (M_{FC}) curve of x = 0.2 shows almost constant magnetization up to 212 K and below, the magnetization increases and achieves maximum magnetization at spin reorientation temperature, T_{SR1} observed at ~70 K. Below T_{SR1}, magnetization decreases abruptly up to 36 K, second spin reorientation temperature, T_{SR2} followed by a slight increase in magnetization down to 2 K. dM/dT with T plot shows the negative kink at around 212 K with zero, rate of change of magnetization at T_{SR1} and T_{SR2} (figure 5.8).

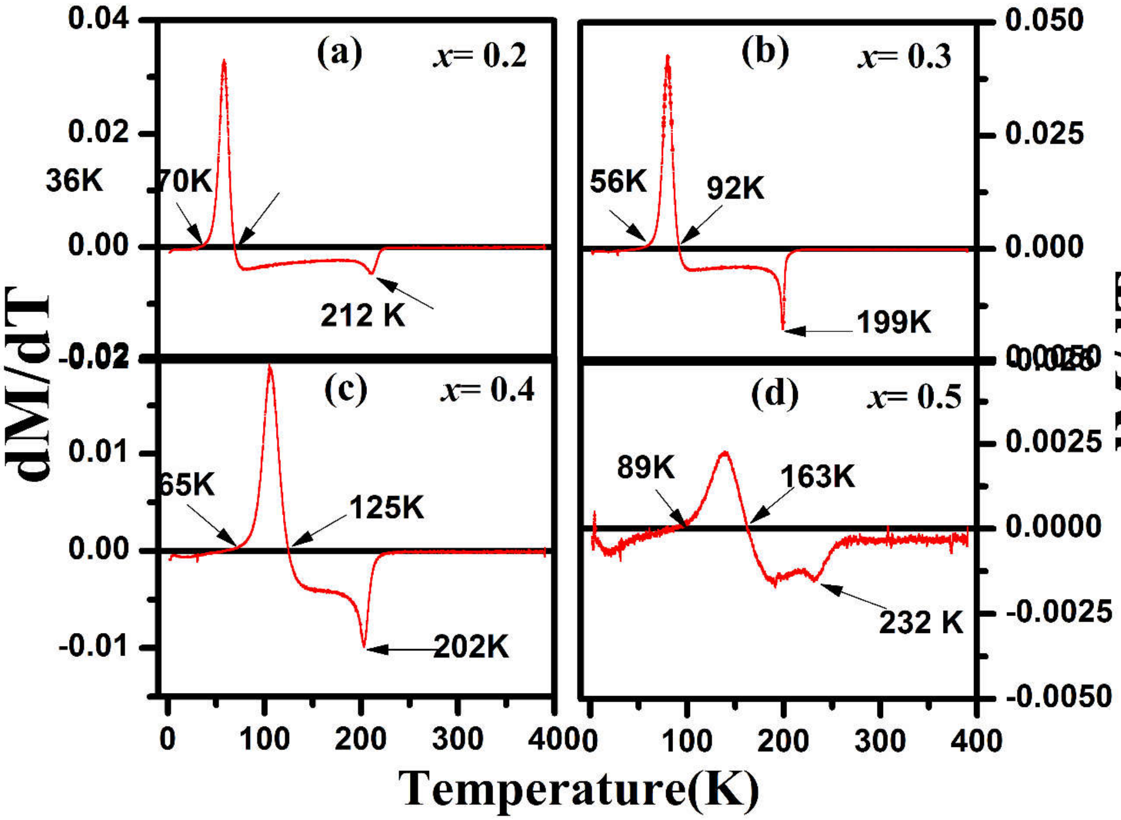

Figure 5.8 dM/dT v/s T plot (dM/dT,first order differentiation of field cooled magnetization with respect to temperature).

In our previous work, we have reported the magnetic properties of $CeCr_{1-x}Fe_xO_3$ (0<x<0.1) nanoparticles. We have shown that the magnetic ordering at 260 K in $CeCrO_3$ due to Cr^{3+}-O-Cr^{3+} antiferromagnetic interaction decreases to ~ 245 K with doping of Fe^{3+} upto at 10 at%. The magnetic ordering above 300 K arises due to Cr^{3+}-O-Fe^{3+} antiferromagnetic interaction showing two spin reorientation temperatures T_{SR1} and T_{SR2}. For $x = 0.1$, Spin reorientation temperatures T_{SR1} and T_{SR2} are reported at 43 K and 26 K, respectively. With increase in x to 0.2 T_{SR1} increased to 70 K and T_{SR2} reaches 36 K at $x = 0.2$. Further, Spin reorientation temperatures, T_{SR1} and T_{SR2} are found to increase from 70 K to 124 K and 36 K to 65 K, respectively, when x increases from 0.2 to 0.4. Change in T_{SR1} and T_{SR2} with increase in Fe concentration are clearly visible from dM/dT vs. T plot. Magnetization vs. temperature behavior for x=0.5 are quite different from $x = 0.2$ to 0.4. Magnetization for ZFC and FC are much higher compared to the magnetization of $x = 0.2$ to 0.4, and its shows a clear bifurcation up to 380 K for $x = 0.5$. Magnetizations vs. temperature behavior of these compositions are further checked under high external applied field i.e. 10 kOe (Figure 5.9). At 10kOe, similar change in T_{SR1} and T_{SR2} are observed with increase in Fe concentration as observed under 0.5 kOe external applied field. T_{SR1} and T_{SR2} increase from 62 K to 138 K and 37 K to 83 K, respectively, with increase in x from 0.2 to 0.5. For $x = 0.5$, ZFC and FC magnetization curve are merged and shows decrease in T_{SR1} to 138K and T_{SR2} to 83K compared to the T_{SR1} and T_{SR2} under 0.5 kOe. At 10kOe, T_{SR1} are slightly decreases, but T_{SR2} slightly increases, compared to the T_{SR1} (165K) and T_{SR2} (86K) at 0.5 kOe external field for all the composition (except $x = 0.5$) as expected. Magnetization at 3K significantly increases with increase in x and it shows higher value compared to magnetization at T_{SR1}. Sharpness of SR between T_{SR1} to T_{SR2} is found to be decreases with increase in x. As we have previously

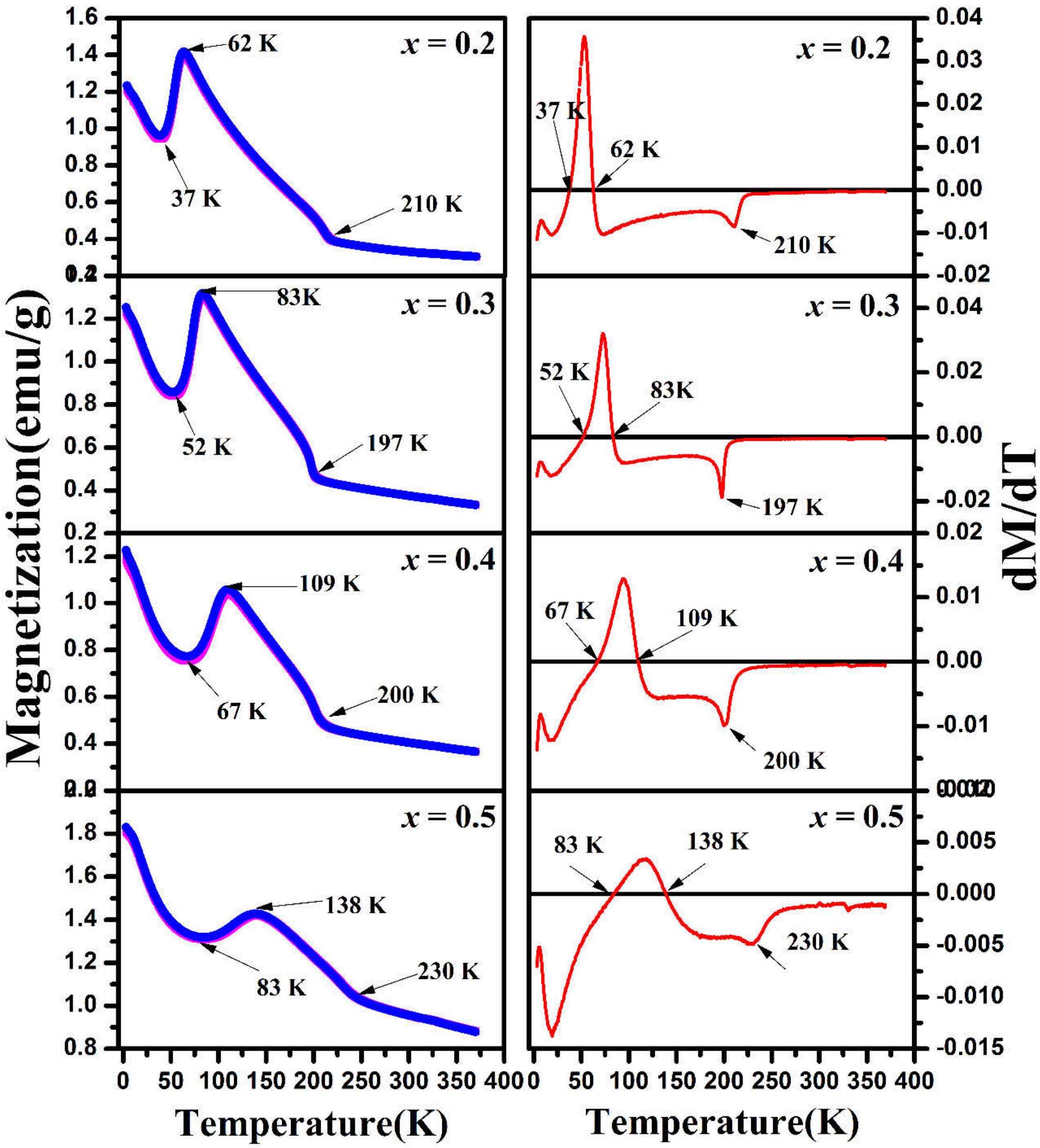

Figure 5.9 Magnetization v/s Temperature plot of $CeCr_{1-x}Fe_xO_3$($0.2 \leq x \leq 0.5$) at 10 kOe in field cooled and zero field cooled mode. And dM/dT v/s T plot (dM/dT, first order differentiation of field cooled magnetization with respect to temperature).

discussed after substitution of Fe, Ce^{3+}–Fe^{3+}/Cr^{3} magnetic interactions are mainly responsible for spin reorientation. But the formation of Fe^{2+} introduced additional magnetic interaction such as Fe^{3+}/Cr^{3+}– Fe^{2+}, Ce^{3+}–Fe^{2+} and Fe^{2+}–Fe^{2+}. Even though the concentration of Fe^{2+} is increases with increase in x, the Fe^{2+}–Fe^{2+} interaction is weak therefore Fe^{3+}/Cr^{3+}–Fe^{2+} and Ce^{3+}–Fe^{2+} interaction play a crucial role on SRT. The study of spin reorientation transition driven by double exchange in $CeFeO_3$ by Li Hou et al. suggest that the spin reorientation in $CeFeO_3$ is mainly governed by Ce^{3+}-Fe^{3+}, Fe^{3+}- Fe^{3+} and Fe^{2+}-Fe^{3+} [95]. The first order spin reorientation in $CeFeO_3$ is attributed to Ce^{3+}-Fe^{3+} FM interaction while as second order spin reorientation temperature is attributed to Fe^{2+}-Fe^{3+} [95]. In as prepared $CeFeO_3$ the first order SRT are sharp and found at 240 K whereas in annelid $CeFeO_3$ with the formation of Fe^{2+} the sharpness of first order SR decrease as well as the SRT decreases to 230 K[95]. Therefore, dilution of Ce^{3+}-Fe^{3+} and Fe^{3+}- Fe^{3+} decreases the SRT and presence of Fe^{2+}-Fe^{3+} FM interaction decreases the sharpness. In $CeCrO_3$ SR are predicted of second order type and mainly responsible due to the antiferromagnetic interaction of Ce^{3+}–Cr^{3+}. Further, Fe substitution upto $x = 0.1$, shows first order type spin reorientation which are attributed to Ce^{3+}–Fe^{3+}/Cr^{3} magnetic interaction, where Ce^{3+}-Fe^{3+} is FM and Ce^{3+}-Cr^{3+} is AFM interaction. With increase in x from 0.2 to 0.5, the magnetic interaction Ce^{3+}-Fe^{3+} and Fe^{3+}- Fe^{3+} with the increase in small amount of Fe^{2+}-Fe^{3+}. Therefore, with increase in x from 0.2 to 0.5, increases in T_{SR1} and T_{SR2} can be attributed to the Ce^{3+}-Fe^{3+} and Fe^{3+}- Fe^{3+} magnetic interaction while as decreases in the sharpness of SR between T_{SR1} and T_{SR2} in $x = 0.5$ can be attributed to Fe^{2+}-Fe^{3+} FM interaction.

5.5.2 Field dependent magnetization

Figure 5.10, 5.11,5.12 and 5.13 depicts the field-dependent isotherms magnetization of $CeCr_{1-x}Fe_xO_3$ ($0.2 \le x \le 0.5$) in the ZFC mode for various temperatures.

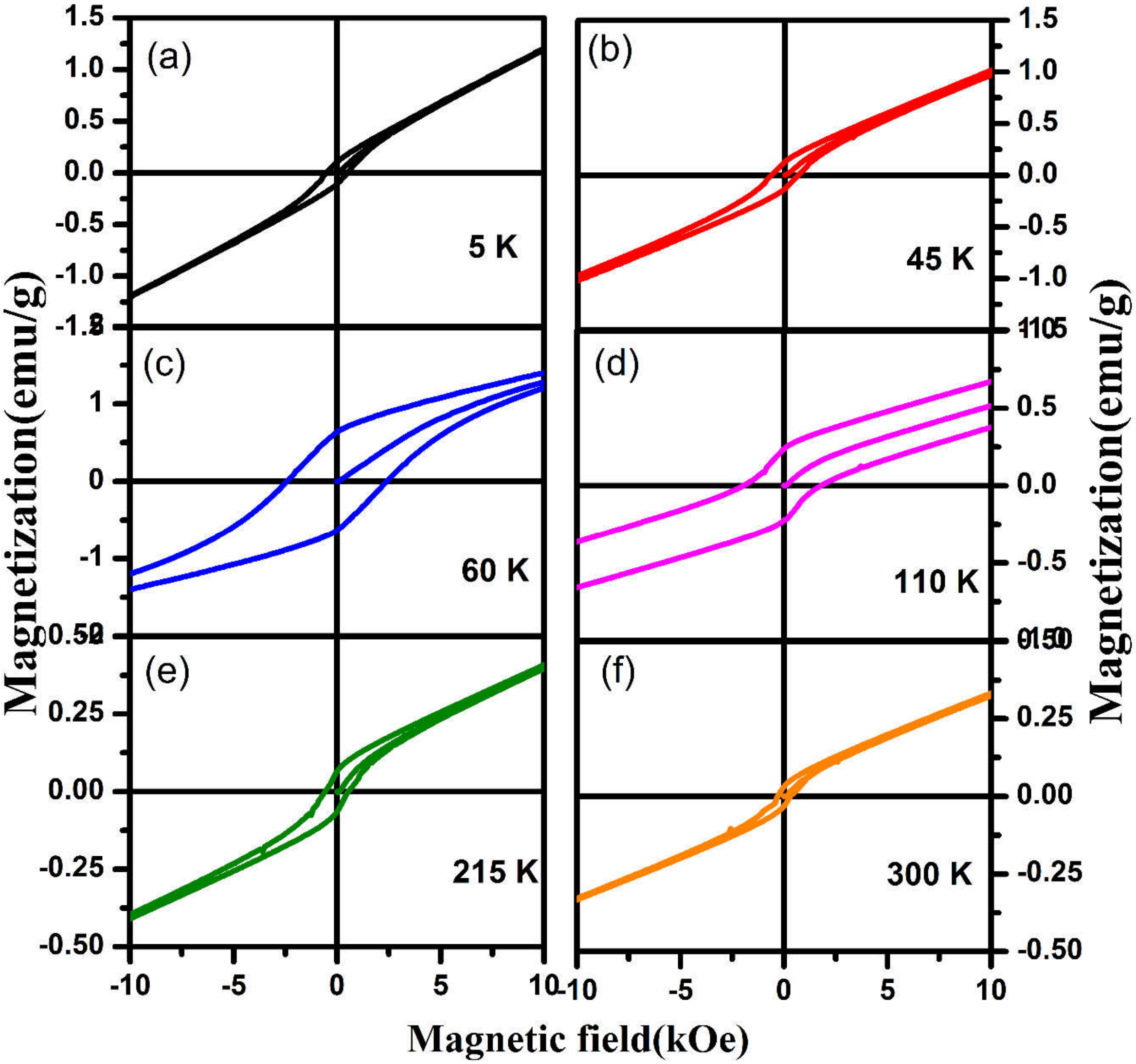

Figure 5.10 Magnetization vs. Field curve of $CeCr_{1-x}Fe_xO_3$ ($x = 0.2$) at 5K, 45K, 60K, 110K, 215 K and 300K.

Figure 5.10 illustrate the magnetization vs. field plot. Hysteresis at 300 K confirm the transition temperature are above room temperature. Further a small hysteresis loop is also observed at 5K with increased magnetization. The hysteresis loop increases with increase in temperature show a broad hysteresis around T_{SR1} ~70K and above this temperature the broadening of hysteresis again decreases.

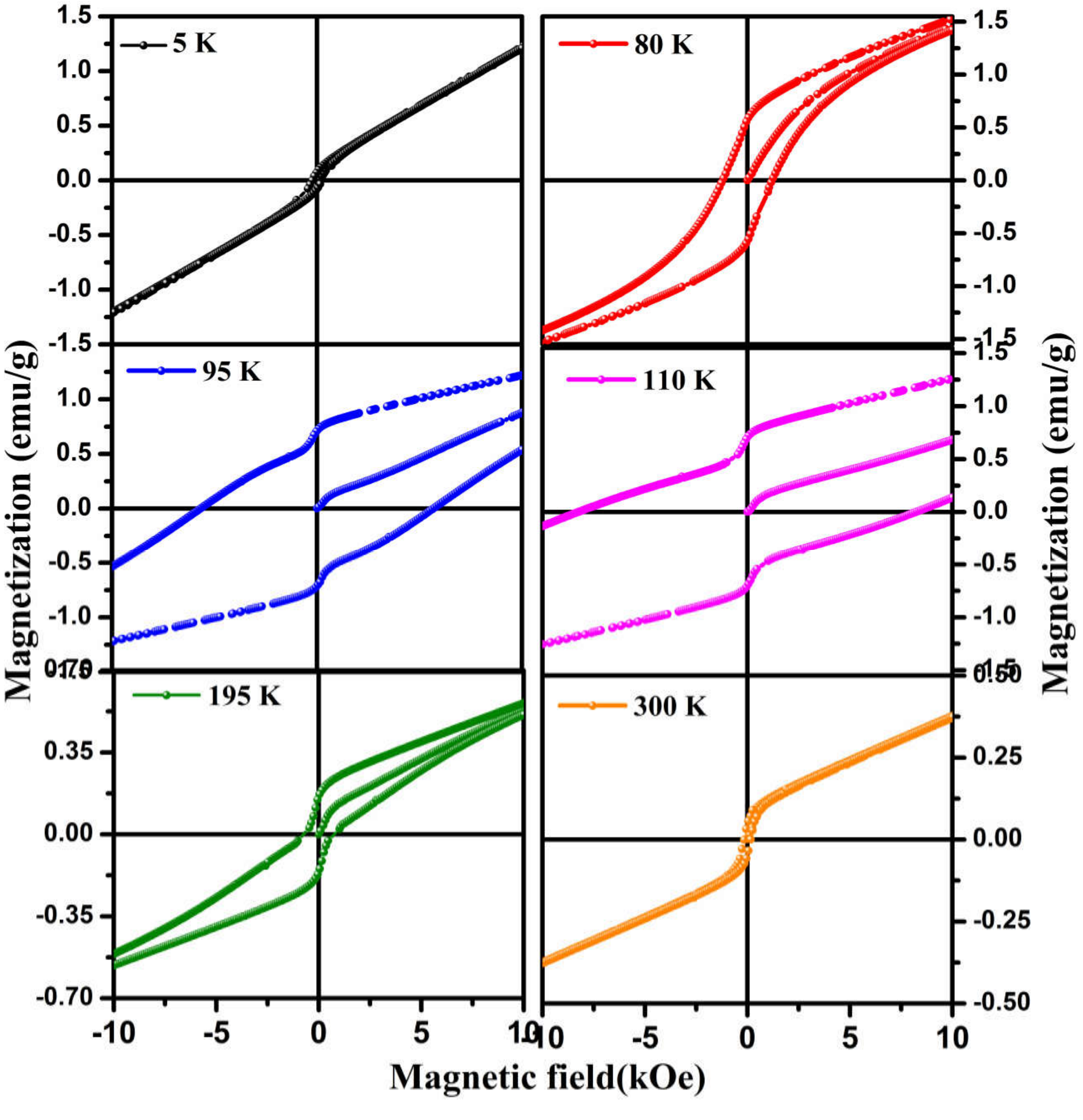

Figure 5.11 Magnetization vs. Field curve of $CeCr_{1-x}Fe_xO_3$ ($x = 0.3$) at 5K, 80K, 95K, 110K, 195 K and 300K.

Moreover, it is also observed that magnetization irrespective of temperature does not saturate. Non saturation behavior is attributed to the antiferromagnetic behavior of the sample. Similar kind of field dependent magnetization behavior is also observed in $x = 0.3$,

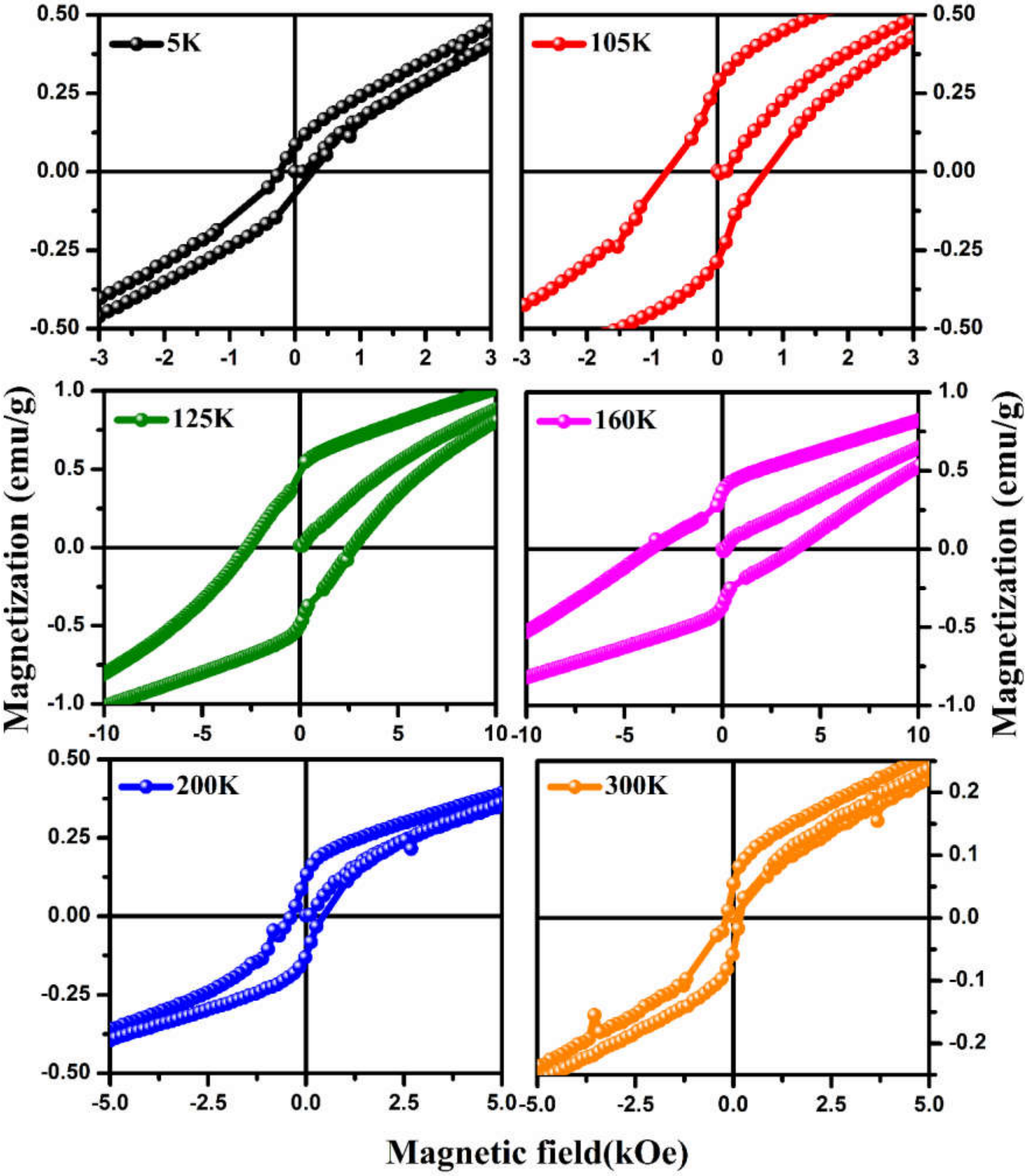

Figure 5.12 Magnetization vs. Field curve of $CeCr_{1-x}Fe_xO_3$ ($x = 0.4$) at 5, 105, 125, 160, 200 and 300 K.

0.4 and 0.5 (figure 5.11,5.12,5.13) with respect to temperature. Coercivity is estimated from M-H loop at each temperature and plotted in figure 5.15 for $x = 0$ to 0.4. For $x = 0.5$ the H_C vs. temperature is depicted in the inset of figure 5.14. For all the composition the highest coercivity are observed around T_{SR1}.

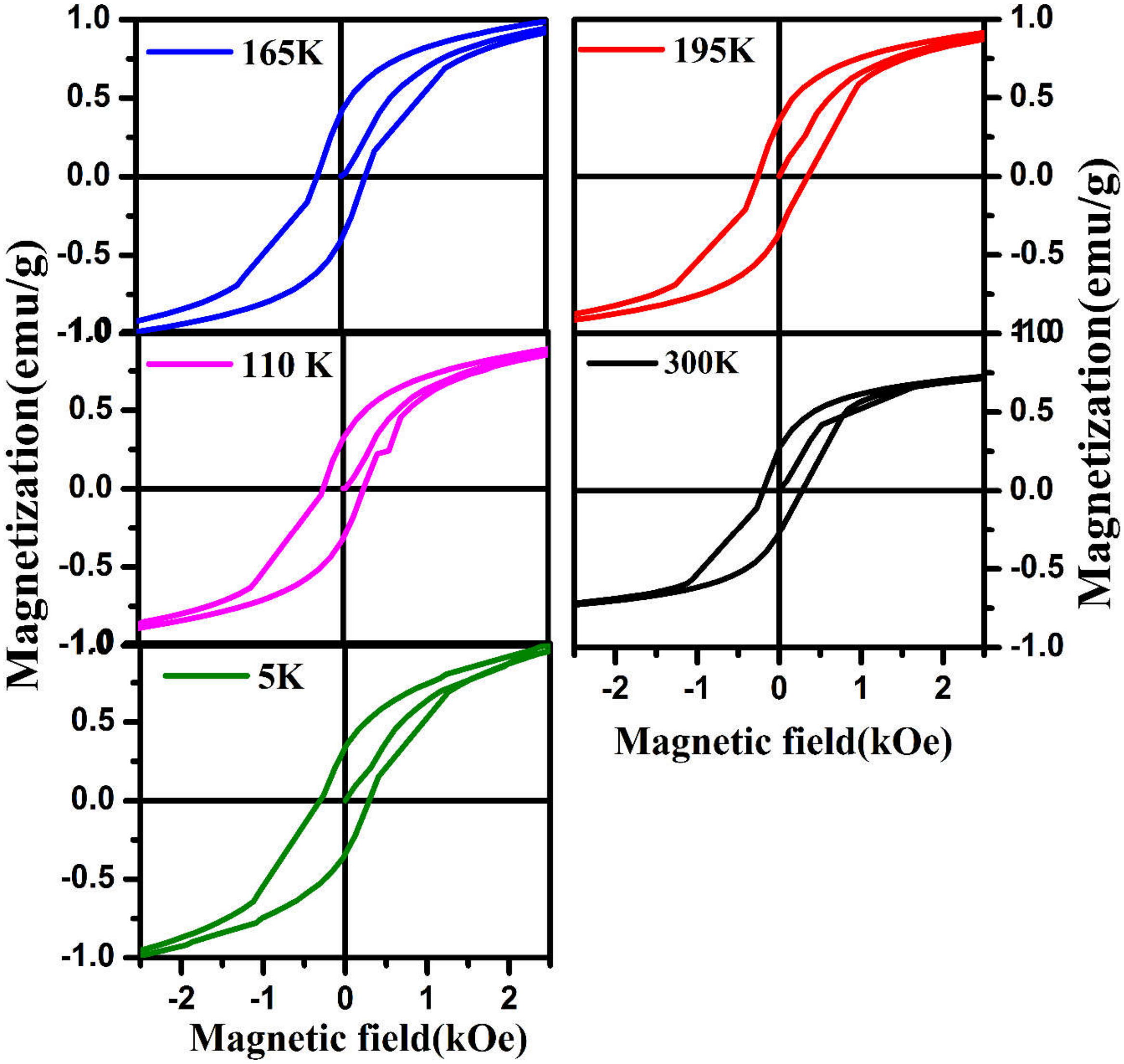

Figure 5.13 Magnetization vs. Field curve of $CeCr_{1-x}Fe_xO_3$ ($x = 0.5$) at 5, 110, 165, 195 and 300K.

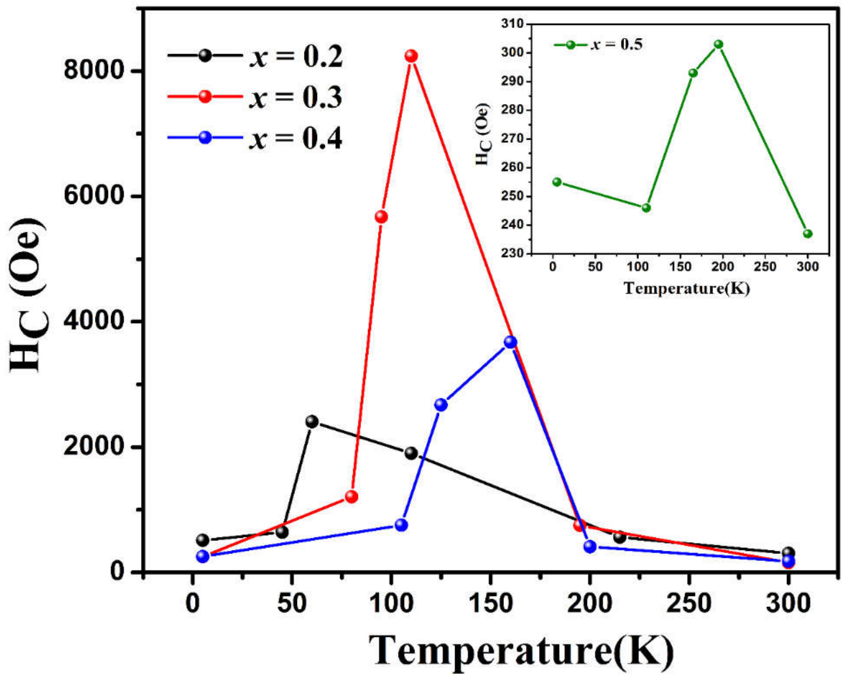

Figure 5.14 Coercivity vs. temperature plot for $CeCr_{1-x}Fe_xO_3$ ($0.2 \le x \le 0.4$). for $x = 0.5$ the plot is shown in inset.

A hysteretic magnetization is observed over the entire SR temperature interval, which is well known indication of a first-order phase transition. Coercivity are found to increase in MH curve when the measurement temperature increases from low temperature (5K) to near T_{SR} and further at higher temperature MH, coercivity again decreases up to 300 K for all the composition. The highest coercivity are observed in $x = 0.3$ at 110 K near T_{SR1}. The magnetization curve shows no perfect saturation established up to 50 kOe. Furthermore, the dc magnetization M increases linearly in the region of larger magnetic field. Low field magnetization loop and its linear change at high field are also attributed to the coexistence of ferromagnetic FM and CAFM state. Magnetization curve are found to be symmetric with the field and magnetization axis, and thus, there is no indication of exchange bias in this system. Generally, the EB effect is observed in samples under field cooled conditions like in $CeCrO_3$ reported by Taheri et. al [91].

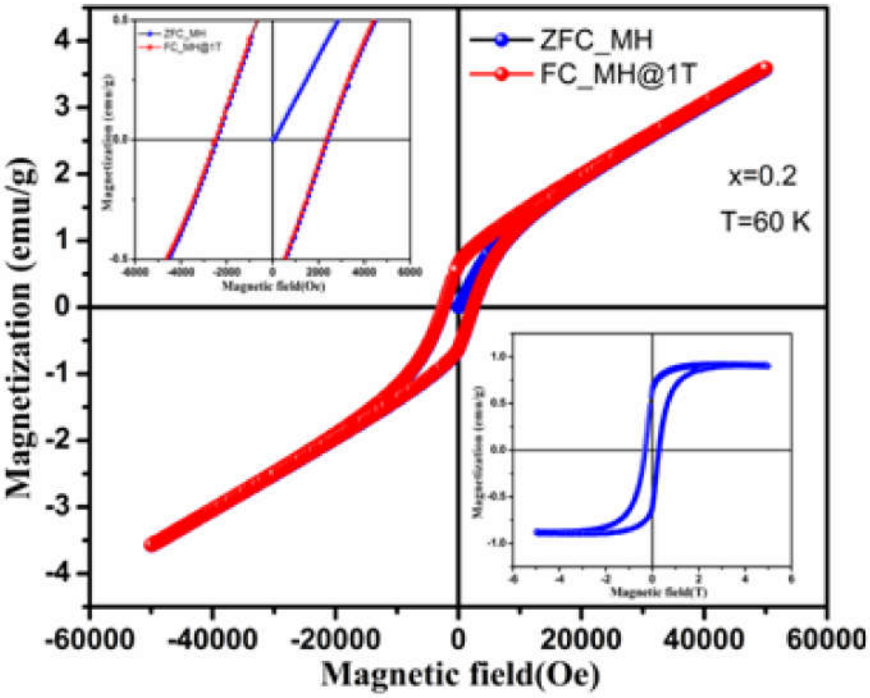

Figure 5.15 Magnetization vs. field plot at 60K of $x = 0.2$ in ZFC and 1T FC mode. After subtracting the antiferromagnetic contribution, the ferromagnetic part is plotted in lower inset. Upper inset shows that there is no exchange bias in MH curve.

Therefore, further measurements in the field cooled mode can only confirm the presence (or absence) of the EB effect in the present compound. We have performed the field cooled (FC) magnetization under 1 Tesla at 60 K, and FC and ZFC magnetization vs. field(MH) plot at 60K are shown in figure 5.15, which shows no significant shift in magnetization curve, indicates no exchange bias are present in this system. At T = 60 K highest coercivity 2.405 kOe are found for $x = 0.2$ and such type of loop are attributed to the coexistence of high field antiferromagnetic (AFM) and low field weak FM states. The total

$M(H)$ behavior of this kind of MH curve can be expressed as $M(H) = \chi_{AF}H + M_s$, where $\chi_{AF}H$ is the antiferromagnetic contribution and M_s is the saturation magnetization of the weak ferromagnetism. Therefore, FM contributed saturated hysteresis loop and corresponding M_s value can be calculated by subtracting the antiferromagnetic contribution from total magnetization (as shown in lower inset of figure 5.15). The high coercivity, H_c= 2.405 kOe, and the saturation magnetization, M_s = 0.9399 emu/g, at T= 60 K are indicative of the FM contribution (figure 5.15). The coercivity are found increase up to $x = 0.3$ and further it starts decreases to $x = 0.5$. The increase and decrease in coercivity of the samples can be understood on the basis of anisotropic and isotropic exchange interaction between Ce^{3+}-Cr^{3+}/Fe^{3+}. In $CeCrO_3$ the interaction between Ce^{3+}-Cr^{3+} are anisotropic and the system shows exchange bias with small hysteric while as in $CeFeO_3$ presence of Ce^{3+}-Fe^{3+} isotropic interaction leads brooder loop in MH with the absence of exchange bias.

5.6 Conclusion

In summary, we synthesized single phase pure, polycrystalline $CeCr_{1-x}Fe_xO_3$ $(0.2 \leq x \leq 0.5)$ using solution combustion method. Rietveld refinement of the XRD pattern confirmed the phase and structure, revealing that the compounds were stabilized in an orthorhombic distorted perovskite structure with a Pnma space group (no-62). With increasing x, The lattice parameter (a, b and c) and volume increases linearly when x increases from 0.2 to 0.5. The increment in lattice parameters and unit cell volume thus suggest that Cr^{3+} ions are replaced by Fe^{3+} ions as the ionic radius increases from 0.615 is Cr^{3+} to 0.645Å is Fe^{3+}. Additionally, the particle size was found to increase with the increase in x. Elemental analysis indicated the formation of Fe^{2+} and Cr^{6+} along with Fe^{3+} and Cr^{3+}, and their formation also increased with the increase in *x*. The band gap decreased from 2.48 to 1 eV as *x* increased, attributed to the increased presence of Fe^{2+}/Fe^{3+} which introduced a trap state in the band gap and reduced its size Furthermore, the spin reorientation temperatures T_{SR1} and T_{SR2} increased from 62 K to 138 K and 37 K to 83 K, respectively, as *x* increased from 0.2 to 0.5. This increase in T_{SR1} and T_{SR2} can be attributed to the enhanced Ce^{3+}-Fe^{3+} and Fe^{3+}-Fe^{3+} magnetic interactions resulting from the substitution of Fe. Coercivity initially increased up to T_{SR1} and then decreased with increasing temperature for all samples. The tuning of the band gap in the visible region, spin reorientation with coercivity, collectively make these materials suitable candidates for photo-catalysis, spintronics, and magnetic switching devices.